Waves, Advection, and Cloud Patterns on Venus

PAUL J. SCHINDER,* PETER J. GIERASCH, STEPHEN S. LEROY AND MICHAEL D. SMITH

Department of Astronomy, Cornell University, Ithaca, New York

(Manuscript received 21 November 1989, in final form 21 February 1990)

ABSTRACT

The stable layers adjacent to the nearly neutral layer within the Venus clouds are found to be capable of supporting vertically trapped, horizontally propagating waves with horizontal wavelengths of about 10 km and speeds of a few meters per second relative to the mean wind in the neutral layer. These waves may possibly be excited by turbulence within the neutral layer. We examine the properties of the waves, and the patterns which they might produce within the visible clouds if excited near the subsolar point. The patterns can be in agreement with many features in images. The waves are capable of transferring momentum latitudinally to help maintain the general atmospheric spin, but at present we are not able to evaluate wave amplitudes. We also examine an alternative possibility that the cloud patterns are produced by advection and shearing by the mean zonal and meridional flow of blobs formed near the equator. We conclude that advection and shearing by the mean flow is the most likely explanation for the general pattern of small scale striations.

1. Introduction

At a height of about 50 km in the Venus atmosphere, where the pressure is about 1 bar and the temperature is about 340 K, there is a turbulent layer about one scale height thick within the thickest region of the Venus cloud deck (Knollenberg et al. 1980). The thermal structure has been probed by the four Pioneer descent vehicles (Seiff et al. 1980) and is very close to adiabatic from 50–55 km, and markedly stable both above and below, with Brunt-Väisälä frequencies on the order of $N = 10^{-2}\ s^{-1}$. Pioneer data (Councelman et al. 1980) also shows that the zonal wind shear is small within the "convection layer" and larger both above and below. Profiles of zonal wind and of N^2, abstracted from the Pioneer data by Young et al. (1987) are displayed in Fig. 1. The key features of the stability and shear structure appear to be permanent. They also appear in USSR descent probe data (Kerzhanovich and Marov 1983). The Soviet/French VEGA balloon floated within the convection layer, and measured a nearly adiabatic thermal gradient together with vertical motions of a few meters per second (Blamont et al. 1986).

Approximately 15 km higher in the atmosphere, between 65 and 70 km elevation, where the pressure is about 50 mb, ultraviolet cloud markings are observed (Kawabata et al. 1980). There is a great deal of imaging data concerning motions and morphology at these levels, with resolutions as low as 20 km (Belton et al. 1976a; Anderson et al. 1978; Rossow et al. 1980). Many of the small scale blotches and striations in the clouds may be due to activity that is seated within the convection layer.

The convection layer, the adjacent stable regions, and the visible cloud tops on Venus form an interesting dynamical region with significant observational documentation. In this paper we examine a number of questions relating to this region and to the imaging observations.

In section 2 we ask whether horizontally propagating, vertically ducted internal waves can be supported in the stable layers adjacent to the convection zone. The answer is yes, but the horizontal wavelengths are too small for comparison with the currently available data. [Evidence for possible ducting of easterly waves at a longer wavelength is given by Hou and Farrell (1987).] Nevertheless, features at visible scales may still be due to breaking events along wave fronts. The wave patterns that would rise are obtained. We discuss the possible importance of these ducted waves to the general circulation. We also show that another class of ducted waves can exist deeper within the Venus atmosphere. These might be excited by convection near the surface.

We do not attempt in this paper to calculate which modes might be driven by the convective zones, or how much energy and momentum is deposited into (or removed from) each mode by convection. Nor do we try to determine whether nonlinear effects on the waves (such as wave breaking) possibly cause observable dissipation into turbulence away from the convective region. All of these effects are currently being investigated by Leroy and Ingersoll (1989).

* Also affiliated with Cornell National Supercomputer Facility.

Corresponding author address: Dr. Paul J. Schinder, Center for Radiophysics and Space Research, Cornell University, 410 Space Sciences Building, Ithica, NY 14853.

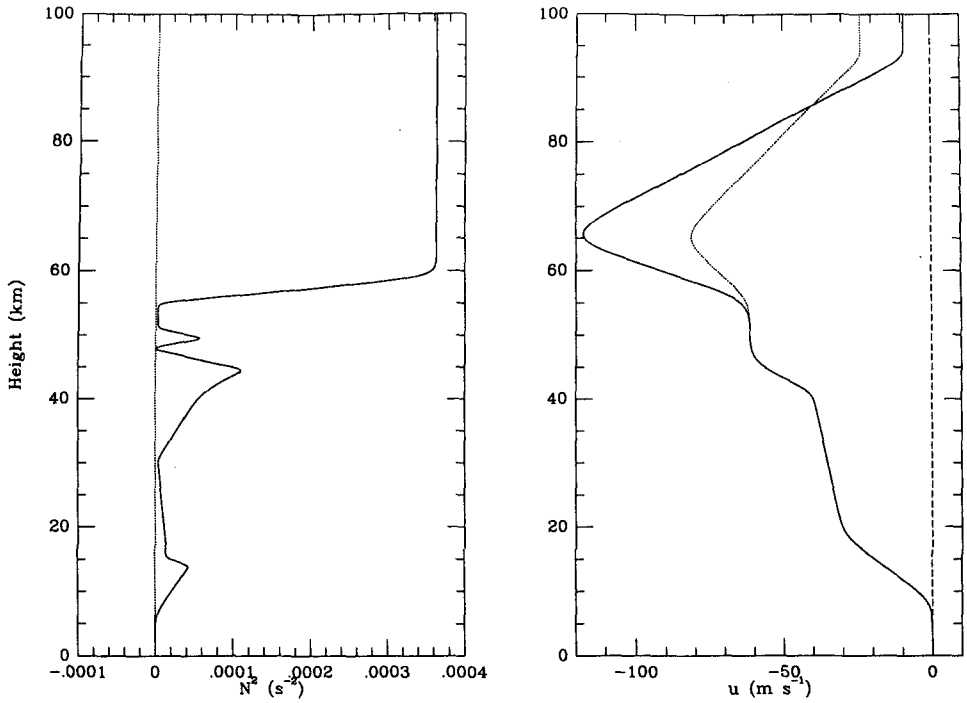

FIG. 1. A plot of the Brunt–Väisälä frequency N^2 and the zonal wind speed $\bar{u}$. These are taken from the basic state fits of Young et al. (1987). The dotted line on the right hand side is the alternative $\bar{u}$ we use in our sensitivity test. This was chosen to be in the range of uncertainty of measured wind velocities above the clouds.

In section 3 we examine another hypothesis for the pattern of striations in the Venus clouds, and show that shear by the mean zonal and meridional circulation near the cloud tops would deform blotches originating at low latitudes into streak patterns like those observed.

In section 4 we summarize our results. Ducted waves near the convection zone cannot be observationally verified with the data at hand, but it is important that the shear and stability structure of the atmosphere can support their existence, and they must be taken into account when considering the cloud region dynamics. Production of the dominant cloud pattern by simple mean flow advection of cloud inhomogeneities appears a viable hypothesis, consistent with observations of both the winds and the streaky patterns.

2. Ducted waves

a. Basic equations

We begin with the hydrodynamic equations in the form

$$\hat{\rho}_{,t} + \nabla\cdot(\hat{\mathbf{v}}\hat{\rho}) = 0$$

$$\hat{\mathbf{v}}_{,t} + \hat{\mathbf{v}}\cdot\nabla\hat{\mathbf{v}} + \frac{\nabla\hat{p}}{\hat{\rho}} = \mathbf{g} + \mathbf{f}$$

$$c_p(\hat{T}_{,t} + \hat{\mathbf{v}}\cdot\nabla\hat{T}) - R(\hat{p}_{,t} + \hat{\mathbf{v}}\cdot\nabla\hat{p}) = q \qquad (1)$$

Here $\hat{\rho}$ is the mass density, $\hat{\mathbf{v}} = (\hat{u}, \hat{v}, \hat{w})$ is the velocity of the fluid, and $\hat{T}$ is the temperature. The pressure $\hat{p} = \hat{\rho}R\hat{T}$, and c_p is the specific heat at constant pressure. The gravitational acceleration is $\mathbf{g} = (0, 0, -g)$ where $g = 8.9$ m s^{-2}. We include on the right hand side the quantities q and $\mathbf{f}$, which are small heating and forcing terms, respectively, and can be used to model small nonlinear effects such as convection. By writing the equations in this form, we assume that the effects of planetary rotation and gas viscosity can be neglected. We use the comma operator for differentiation: $f_{,x} \equiv \partial f/\partial x$.

We now write $\{\hat{\rho}, \hat{u}, \hat{v}, \hat{w}, \hat{T}\} = \{\bar{\rho}, \bar{u}, \bar{v}, \bar{w}, \bar{T}\} + \{\rho, u, v, w, T\}$. The barred quantities are time independent solutions of (1) with $q = 0$ and $\mathbf{f} = 0$, and $\{\rho, u, v, w, T\}$ are small perturbations around this base state. We set $\bar{v} = \bar{w} = 0$, which means $\bar{p}_{,z} = -g\bar{\rho}$ and $\bar{p}_{,x} = \bar{p}_{,y} = 0$. The quantities $\bar{u}(z)$, $\bar{T}(z)$, and $\bar{\rho}(z)$ are obtained from an analytic approximation to the mean structure of the Venusian atmosphere given by Young et al. (1987).

We provide details of the derivation of the wave equation in the Appendix; here we will just sketch the procedure. We expand (1) to first order in the small quantities. We successively eliminate ρ, u, v, and T from the set of equations, leaving two coupled equations in p and w. We next write $p(z, x, y, t) = \int p(z, k_x, k_y, \omega)e^{ik_x x + ik_y y - i\omega t}dk_x dk_y d\omega$, and similarly for ω, $\mathbf{f}$,

and q. We proceed using the Fourier components $p(z, k_x, k_y, \omega)$ and $w(z, k_x, k_y, \omega)$, eventually arriving at

$$\psi_{,zz} + G\psi = F, \tag{2}$$

where $\psi \equiv (D^2/\mathcal{D}\bar{\rho})^{1/2}(\bar{\rho}w/D)$, $D = -i(\omega - \bar{u}k_x)$, and $\mathcal{D} \equiv -k_x^2 - k_y^2 - D^2/c^2$. In (2)

$$G = \frac{N^2 - \tilde{\omega}^2}{\tilde{\omega}^2}k^2 + \frac{\tilde{\omega}^2}{c^2} - \frac{N^2}{g}\frac{X_{,z}}{X} + \frac{N^2_{,z}}{g} - \frac{1}{4}\left[\frac{\bar{\rho}_{,z}}{\bar{\rho}} + \frac{X_{,z}}{X}\right]^2 + \frac{1}{2}\left[\frac{\bar{\rho}_{,z}}{\bar{\rho}} + \frac{X_{,z}}{X}\right]_{,z} \tag{3}$$

where $\tilde{\omega} = \omega - k_x\bar{u}$, $X = (k^2/\tilde{\omega}^2 - 1/c^2)$, $k^2 \equiv k_x^2 + k_y^2$, and

$$F = \left(\frac{X}{\bar{\rho}}\right)^{1/2}\left\{\frac{\bar{\rho}gq}{D\bar{T}} + \bar{\rho}f_z - \left(\frac{g}{c^2} + \frac{\partial}{\partial z}\right)\left[\frac{i\bar{\rho}}{\mathcal{D}}(k_xf_x + k_yf_y) - \frac{\bar{\rho}Dq}{\mathcal{D}\bar{T}}\right]\right\}. \tag{4}$$

It is useful to rewrite (3) as

$$G = \frac{1}{\tilde{\omega}^2}(N^2k^2) + \frac{1}{\tilde{\omega}}\left[\left(\frac{N^2}{g} - \frac{g}{c^2}\right)\frac{d\tilde{\omega}}{dz} + \frac{1}{a}\frac{da}{dz} - \frac{d^2\tilde{\omega}}{dz^2}\right] - k^2 + \frac{\tilde{\omega}^2}{c^2} - \frac{N^2}{g}\frac{1}{a}\frac{da}{dz} - \frac{1}{4}\left[\frac{1}{\bar{\rho}}\frac{d\bar{\rho}}{dz} + \frac{1}{a}\frac{da}{dz}\right]^2 + \frac{1}{2}\frac{d}{dz}\left[\frac{1}{\bar{\rho}}\frac{d\bar{\rho}}{dz} + \frac{1}{a}\frac{da}{dz}\right] + \frac{N^2_{,z}}{g} \tag{5}$$

where $a \equiv (1 - \tilde{\omega}/k^2c^2)$. Note that as $\omega \to k_x\bar{u}$, $\tilde{\omega} \to 0$ and $G \to \infty$. For a given (k_x, k_y, ω), the values of z, if any, at which $\tilde{\omega} = 0$ we denote *critical levels*. Near the critical level, the behavior of $G(z)$ may be determined by expanding $1/\tilde{\omega}^2$ in a Taylor series, to obtain

$$G \sim \frac{N^2k^2\left(\frac{d\tilde{\omega}(z_0)}{dz}\right)^{-2}}{(z - z_0)^2} \tag{6}$$

where z_0 is the position of the critical level.

Assuming $G = A/(z - z_0)^2$, where A = constant, an analytic solution to (2) may be found:

$$\psi = \Psi_+(z - z_0)^{\alpha_+} + \Psi_-(z - z_0)^{\alpha_-} \tag{7}$$

where $\Psi_\pm$ are constants and $\alpha_\pm = 1/2 \pm i(A - 1/4)^{1/2}$. This simple linear theory predicts that $\psi \to 0$ at the critical levels. The actual behavior of the gas is more complicated, since our simple linear theory breaks down near the critical levels. We will always assume, however, that critical levels act as sinks of energy, and will treat critical layers as boundaries which absorb but do not emit energy.

b. Numerical methods

We difference (2) on a uniform grid in z, and solve the resultant complex tridiagonal matrix by well known methods (Press et al. 1986). The boundary conditions we use depend on whether or not critical levels exist for a given (k_x, k_y, ω). If there are no critical levels, then we integrate (2) from the ground, where we set $\psi = 0$, to the "sky" at 100 km, where an outgoing radiation condition is imposed: $d\psi/dz = -i\sqrt{G}\psi$. Because of the nature of the basic state, G is always constant at high altitude, and this is an excellent approximation.

If one or more critical layers exist, then we use a WKB approximation at a point near the singular layer: $d\psi/dz = \pm i\sqrt{G}\psi$. (We typically use an offset from the singular layer of 0.1 km; the solutions only depend very weakly on the exact value.) The sign is chosen to ensure that the singular point does not radiate but only absorbs energy. Note that very near a critical layer, where $G \approx A/(z - z_0)^2$ and ψ is given by (7), the WKB approximation is nearly exact if one of $\Psi_\pm$ is zero and A is large, which is usually the case. We found that the WKB approximation gave better numerical results than (7) or its derivative in regions where A was large. A schematic diagram of the three possibilities is shown in Fig. 2.

To test our code, we constructed a simple G which has many of the features of the G's we find from (5) and for which an analytic solution to (2) may be obtained. The agreement between the analytic solution and the numerical solution was found to be good with maximum errors $\approx$ 5% for 8000 numerical zones in z.

c. Results

We now turn to the results we obtained using the basic state of Young et al. (1987) in (5) to determine $G(z, k_x, k_y, \omega)$. Figure 1 shows $N^2(z)$ and $\bar{u}(z)$. Note the existence of two possible regions of convection, one a few kilometers wide centered at about 52 km, and one at the surface. Depending on the exact structure of G, we will place our forcing term F in one of these regions. In order to reduce the number of free parameters, we always choose $\omega = Ck_x$, where C is a

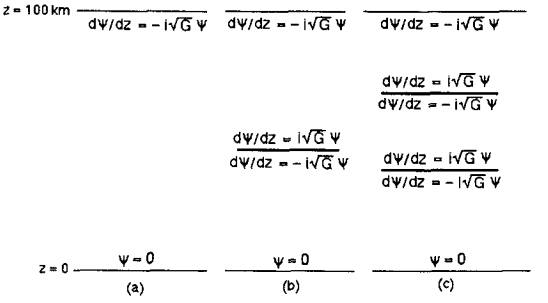

FIG. 2. A schematic diagram of the three possible situations, with either (a) zero, (b) one, or (c) two critical levels. Critical levels are denoted by heavy solid lines. On either side of the critical level, and at the surface and "sky" at z = 100 km, we give the boundary condition we use for numerical computations. We solve (2) only in the region containing the forcing F.

velocity (not to be confused with the sound speed c) chosen to be within ± 5 m s^{-1} of $\bar{u}$ in a convective region. This choice of ω has the great advantage that the critical layers remain fixed for a given choice of C, and makes interpretation of the results easier.

To drive the solutions, we replace (4) by the simple function

$$F(z, k_x, k_y, \omega) = F_0 \exp\left[\frac{-(z - z_l)^2}{\Delta z^2}\right], \quad (8)$$

and calculate the response of the atmosphere to this sharp forcing. Here F_0 is an arbitrary constant, the center of the gaussian is put in one of the convective regions, and Δz is usually 1 km. The results we present below are only weakly dependent on the exact values of z_l or Δz, or in fact on the actual functional form of the forcing.

Figure 3 shows a contour plot of $\log|\psi|_{max}$ on a uniform 64×64 grid in (k_x, k_y) with $0 \leq k_y \leq 10^{-5}$ and $-10^{-10} \geq k_x \geq -10^{-5}$, for $C = -57$ m s^{-1}. In this case, $z_l = 55$ km and $\Delta z = 1$ km. The critical levels occur at $z \approx 45$ km and at $z \approx 82$ km. The forcing drives the wave between these two critical levels. This case is important because the waves will exist in the cloud deck. The quantity $|\psi|_{max}$ is the maximum value of $|\psi|$ anywhere on the grid. In order to guard against finite grid effects, each solution was computed twice on grids of different resolution. For example, the first sweep through the grid was done with grids of 1500 and 2000 at uniformly spaced points in z. If the solutions found on the different grids were within 10% of each other, the solution found on the higher resolution grid was accepted; otherwise, a new solution was attempted with a much higher resolution, typically 20 000 and 15 000 zones. Clearly evident in Fig. 3 are the existence of two ridges, which indicate the existence of resonant modes. There is also the hint of additional ridges at smaller values of k_x.

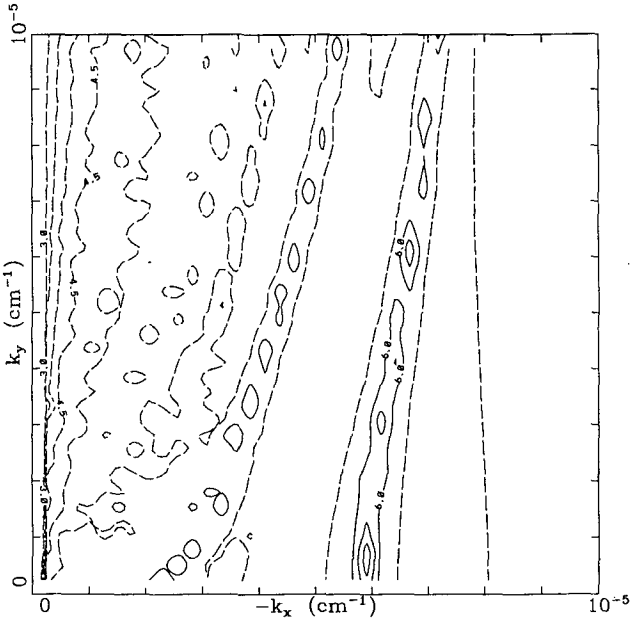

FIG. 3. A contour plot of $\log|\psi|_{max}$ as a function of $-k_x$ and k_y for $C = -57$ m s^{-1}. The quantity $|\psi|_{max}$ is the maximum value of $|\psi|$ at any value of z on the grid. A uniform grid in $-k_x$ and k_y was used, with 64 values in each direction. Contours of $\log|\psi|_{max} < 6$ are shown as dashed lines, while contours of $\log|\psi|_{max} \geq 6$ are shown as solid lines. Clearly evident are two ridges, with traces of a third. Much of the structure is due to the finite (k_x, k_y) grid used. The maximum value of $\log|\psi|_{max} = 8.58$ occurs at $k_x = -5.87 \times 10^{-6}$, $k_y = 6.34 \times 10^{-7}$.

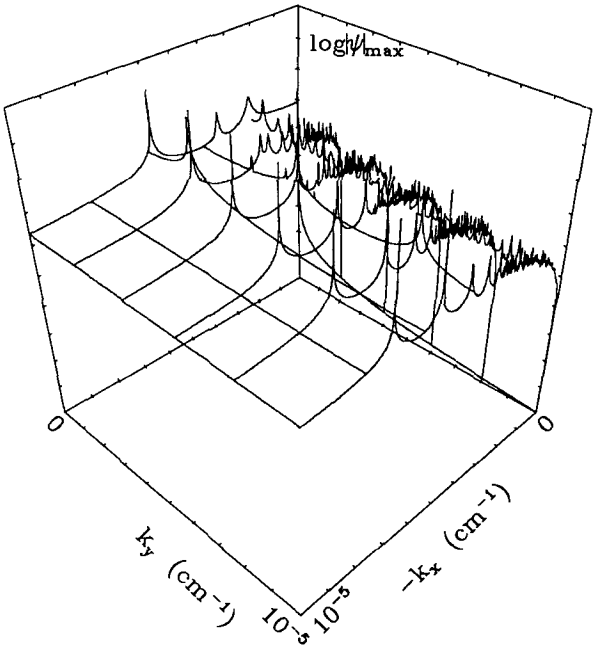

FIG. 4. A plot of $\log|\psi|_{max}$ for $C = -57$ m s^{-1}. Six lines of constant $-k_x$, ($k_x = -10^{-10}, -\{2, 4, 6, 8, 10\} \times 10^{-6}$ cm^{-1}), and six lines of constant k_y ($k_y = \{0, 2, 4, 6, 8, 10\} \times 10^{-6}$ cm^{-1}) are shown. Resolution along the lines is such that the fundamental and first harmonic fully resolved. Several thousand points are used along each line. In this plot $\log|\psi|_{max}$ is normalized to its maximum value.

Much of the structure in Fig. 3 is due to the finite number of points in the 64×64 grid. Fig. 4 is a map of $\log|\psi|_{max}$ in the same region in k_x, k_y space for $C = -57$ m s^{-1}. This time, instead of computing $|\psi|_{max}$ on a uniform grid, we computed it on widely separated lines of constant k_x or k_y, with enough resolution to resolve the peak for the fundamental mode and the first harmonic on all the lines (there are several thousand points on most of the lines). The true sharpness of the resonances is clearly evident, as is the structure due to the higher harmonics for smaller values of k_x.

What causes these resonances? Fig. 5 is a plot of the line $k_x = 4 \times 10^{-6}$ cm^{-1} for $C = -57$ m s^{-1}, and Fig. 6 shows plots of $G(z)$ and $\psi(z)$ for the first two resonances. It is useful to think of G as the negative of a potential; then the left hand side of (2) is the same as

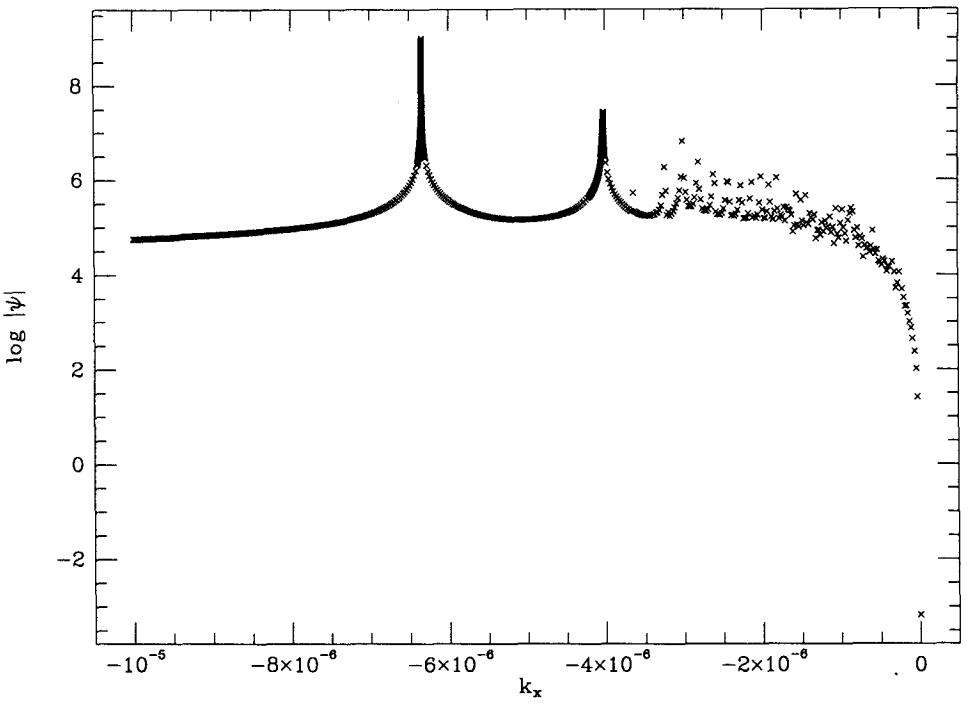

FIG. 5. The line $k_y = 4 \times 10^{-6}$ cm^{-1} for $C = -57$ m s^{-1}.

the Schrödinger equation and useful analogies may be drawn from quantum mechanics. Note that at about 55 km G becomes locally positive, and forms a *duct* (a local "potential well"). The wave can maintain itself in the duct for a long time against the losses occurring into the critical level or to the "sky."

In Fig. 6, we see that G in these plots closely tracks the bahavior of N^2 shown in Fig. 1. Alghough $G(5)$ is a complicated function of z, k_y, and k_x, we can extract the general features of the atmospheric structure which cause the duct, because we find that $G \approx k^2(N^2/\tilde{\omega}^2 - 1)$ is a good approximation to (5). In order to form a duct, we need a region where G is locally positive surrounded by two regions where G is locally negative, to trap the wave. One side of the duct, therefore, is formed by the convective region. G will become positive whenever $N^2 > \tilde{\omega}^2$, and will become negative again whenever this inequality is reversed. Since N grows rapidly in the region of static stability, the first can easily occur. Eventually, though, N stops growing. The quantity $\bar{u}$ continues to change rapidly, since the region of large static stability can support large shears, and eventually $\tilde{\omega}^2 > N^2$. The other side of the duct is formed where this occurs.

Armed with this knowledge, we can now construct a simple model which explains the shape of the resonant peaks in (k_x, k_y) space. We assume that N changes discontinuously at z_1 from 0 to N_1, and remains at the constant value N_1 for all $z > z_1$. We also assume that $\bar{u}_{,z}$ is constant for $z > z_1$. We write $G = k^2(N^2/\tilde{\omega}^2 - 1)$ for $z - z_1$. Then

$$G = k^2\left[\frac{N_1^2}{k_x^2[C - \bar{u}(z_1) - \bar{u}_{,z}(z - z_1)]^2} - 1\right]$$
$$= k^2\left[\frac{\mathrm{Ri}_1}{k_x^2(z_0 - z)^2} - 1\right], \qquad (9)$$

where $z_0 = [C - \bar{u}(z_1)]/\bar{u}_{,z}$ and $\mathrm{Ri}_1 = N^2/\bar{u}_{,z}^2$ is the Richardson number. We compute the phase change Φ between the walls of the "potential well" according to the WKB approximation

$$\Phi = \int_{z_2}^{z_1} \sqrt{G(z)}\, dz, \qquad (10)$$

where z_2 is defined by $G(z_2) = 0$. This integral may be done analytically, and we get

$$\Phi = -\frac{k}{|k_x|}\sqrt{\mathrm{Ri}_1}\left[\ln\left(\tan\frac{\theta}{2}\right) + \cos\theta\right], \qquad (11)$$

where $\sin\theta = |k_x|[\bar{u}(z_1) - C]/N_1$. Whenever $\Phi = (n + \frac{1}{2})\pi$, a bound state (resonant mode) will exist. Fig. 7 is a contour plot of Φ, for the particular values $[\bar{u}(z_1) - C]/N_1 = 10^5$ cm, Ri = 36. Note how remarkably similar this is to the contour plot of resonant peaks shown in Fig. 3.

We also checked the sensitivity of our results to the specific details of the basic state by looking for resonant modes using the alternative velocity profile shown as the dotted line on the right hand side of Fig. 1. This alternative velocity profile was constructed to be within the uncertainties of the measured wind velocities above

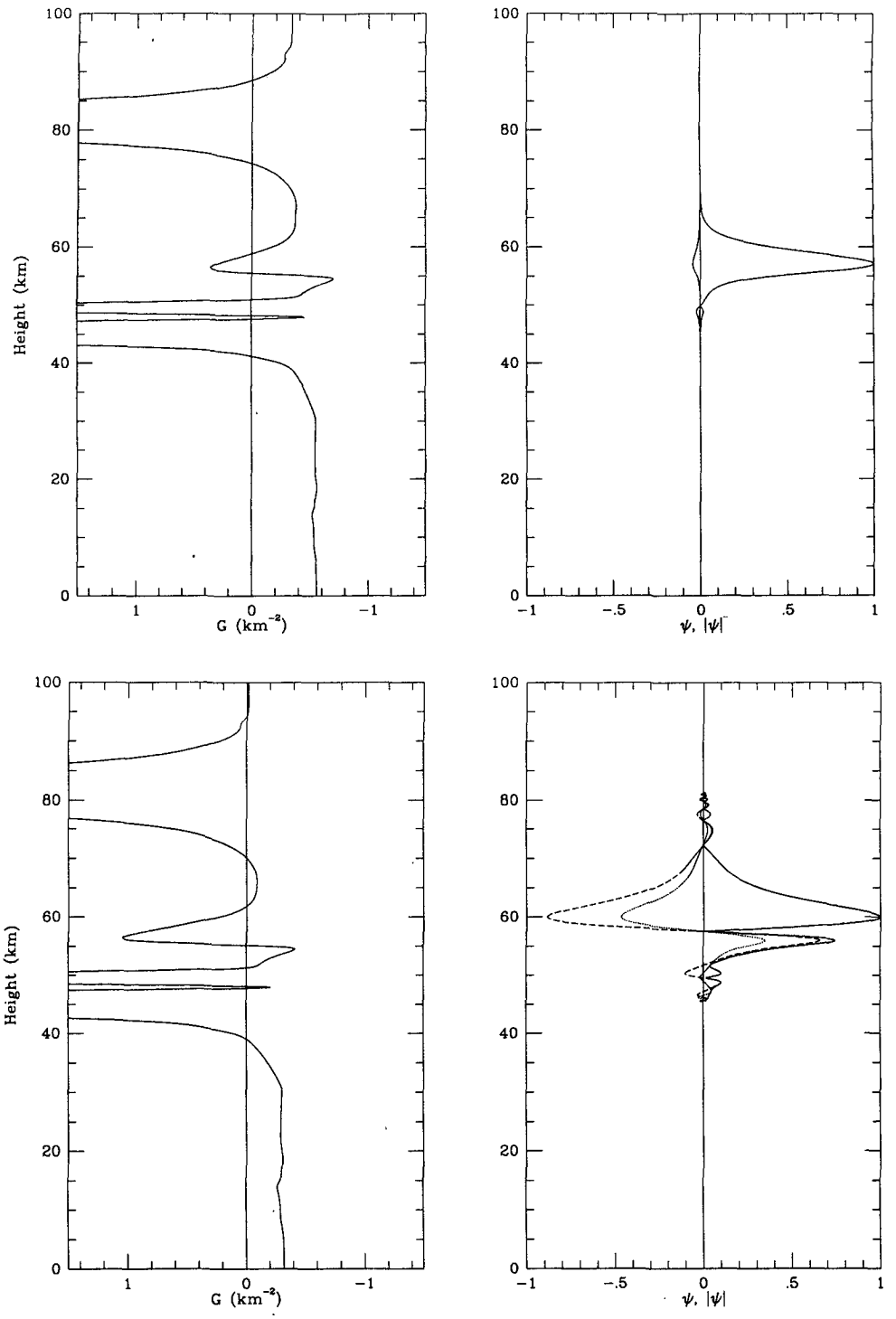

FIG. 6. Plots of $G(z)$ (left) and $\psi(z)$ (right) for the first two resonances for $C = -57$ m s^{-1}, $k_y = 4 \times 10^{-6}$ cm^{-1}: (a) the fundamental at $k_x = -6.34 \times 10^{-6}$ cm^{-1}, (b) the first harmonic at $k_x = -4.03 \times 10^{-6}$ cm^{-1}. In the right plots, the solid line is $|\psi|$, the dahsed line is Re$\{\psi\}$ and the dotted line is Im$\{\psi\}$. The plots on the right are normalized to the maximum value of (a) $|\psi| = 1.04 \times 10^9$, and (b) $|\psi| = 2.56 \times 10^7$.

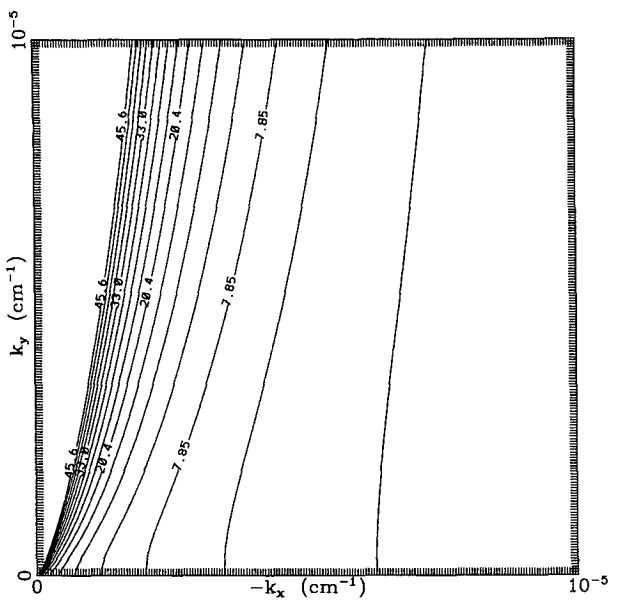

FIG. 7. A contour plot of Φ (11). Compare this with Fig. 3. Contours are drawn where $\Phi = (n + \frac{1}{2})\pi$.

the clouds, where the duct for the $C = -57$ m s^{-1} case occurs. The resonant modes are shown in Fig. 8. No attempt has been made to resolve any of the peaks fully. In general, the structure of the modes is similar to Fig. 4, although they have moved to greater values of $-k_x$. This can be understood qualitatively in terms of our simple model. The change in the velocity profile effectively increases the Richardson number by about a factor of 4, because $\bar{u}_{,z}$ decreases in magnitude, while the value of z_0 is changed by a smaller amount, since $C - \bar{u}(z_1)$ also decreases. Consider the case $k_y = 0$. Then, in order to maintain the same value of the vertical wave number $\sqrt{G}$ (or more precisely, the same $\int \sqrt{G}dz$), $k^2 = k_x^2$ must increase. The size of the increase is uncertain, since both Ri_1, z_0, and the size of the duct are changed, and also because it is unclear how to choose parameters for our simple model to compare with the exact results. The tendency for $-k_x$ to increase, however, is understandable. Both this case and the results of our simple WKB analysis show that the resonant modes are not due to some specific detail of the basic state used in the other cases.

Fig. 9 is a close up of the fundamental mode peak in Fig. 5. The solid line is a fit of this peak to a Lorentz function:

$$|\psi| = \frac{\psi_0 \sigma^2}{(k_x - k_{x0})^2 + \sigma^2}. \qquad (12)$$

The goodness of the fit shows that these resonances take the form of classic wave resonances. The Q of the resonance may be defined as $Q = |k_{x0}|/\sigma$.

Figure 10 is a plot of $\log|\psi|_{\max}$ for $C = -67$ m s^{-1} and $C = 5$ m s^{-1}. The singular layers for $C = -67$ m s^{-1} are at $z \approx 40$ km and $z \approx 57$ km. These waves will not be visible at the cloud tops. There are no singular layers for $C = 5$ m s^{-1}. The same type of resonant behavior is seen in both cases. Ducting in the case $C = -67$ m s^{-1} occurs below the upper convective region. Ducting in the case $C = 5$ m s^{-1} occurs deep in the atmosphere just above the lower convective region at the surface.

What do these waves look like in configuration space? We do not have sufficient detail on any of these maps to perform a fast Fourier transform numerically, so we resort to approximate methods to perform the Fourier transform to find $\psi(x, y, z)$. We assume that $t = 0$, and that the resonant ridge can be well approximated by the δ function $\delta(k_x - k_x(k_y))$, where $k_x(k_y)$ is the position of the peak of the resonance in (k_x, k_y) space. Furthermore, we approximate the function $k_x(k_y)$ by a series of straight line segments. Then the integrals may be performed analytically and we find

$$\psi(x, y, z) = \sum_j e^{-iB_j x}\left[\frac{e^{-ik_{y_{j+1}}X_j} - e^{-ik_{y_j}X_j}}{-iX_j}\right], \qquad (13)$$

where

$$X_j = A_j x + y,$$
$$A_j = (k_{x_{j+1}} - k_{x_j})/(k_{y_{j+1}} - k_{y_j}),$$
$$B_j = (k_{y_{j+1}}k_{x_j} - k_{y_j}k_{x_{j+1}})/(k_{y_{j+1}} - k_{y_j}), \qquad (14)$$

and the index j denotes the individual line segments.

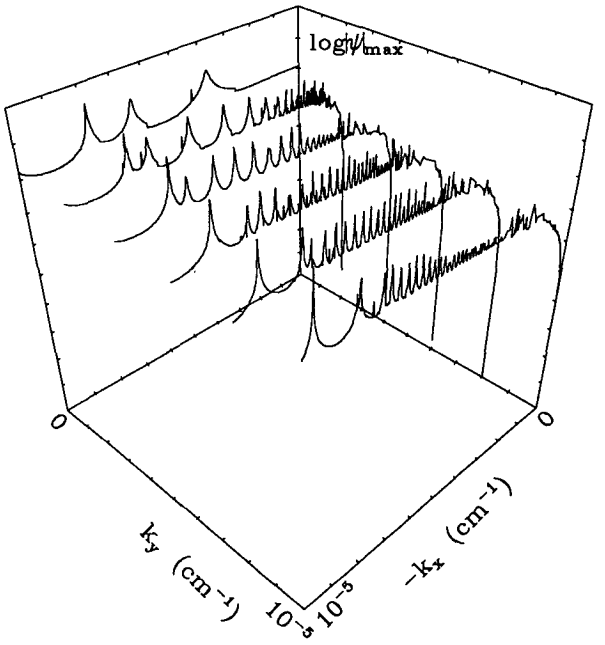

FIG. 8. A plot similar to Fig. 4 for the alternative velocity profile shown as the dotted line in Fig. 1.

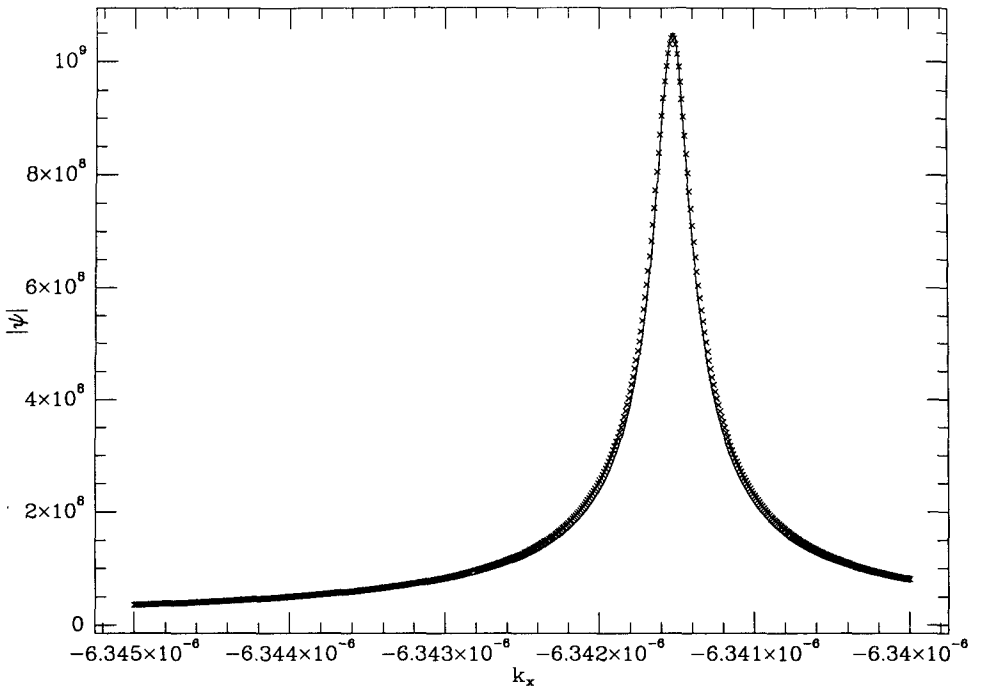

FIG. 9. A close up of the fundamental peak at $k_x = -6.34 \times 10^{-6}$ cm^{-1} for $C = -57$. The ×'s mark the numerical solutions. The solid line is the best fit Lorentzian, with $\psi_0 = 1.05 \times 10^9$, $\sigma = 1.1 \times 10^{-10}$ cm^{-1}.

Figure 11 shows $\mathrm{Re}\{\psi(x, y, z)\}$ for the $C = -57$ m s^{-1} case for the region $0 < x < 200$ km and $-100 < y < 100$ km. The forcing F is applied at $x = 0$, $y = 0$. Clearly evident is the V-shaped wake pattern shown by Gierasch (1987). The narrowness of the wave pattern can be understood by using the method of stationary phase: the wave crests in configuration space should lie along lines such that $x/y = dk_y/dk_x$. Since dk_y/dk_x is large, small increases in y lead to large increases in x.

d. General circulation speculations

To maintain the general circulation of the Venus atmosphere, the atmosphere at low latitudes near the cloud level must be accelerated by waves, tides or some other longitudinally varying flow component. The transfer must be either horizontally from higher latitudes or vertically from deep levels near the surface. As yet, the particular processes at work have not been definitively identified. Schubert (1983) reviews the situation. It is conceivable that small scale waves play a part. If horizontally ducted waves are to accomplish an important transfer of momentum from high latitudes, three questions must be answered. Why should waves transfer momentum in this particular direction? Can waves propagate several thousand kilometers? Is the magnitude of the acceleration that they can produce of sufficient amplitude?

Both eastward and westward waves (relative to the local flow) can be ducted, eastward ones above the convection zone and westward ones below. At those times when westward jets exist at high latitudes, the westward waves will be refracted back toward the equator by the latitudinal shear because the wave phase speed is its intrinsic speed plus the mean flow speed. Recall that we are speaking of waves with intrinsic speeds of a few meters per second, and a midlatitude jet of tens of meters per second, so refraction is a strong effect. On the other hand, eastward waves are refracted more poleward by such a shear, and can penetrate to high latitudes, eventually to be absorbed. This qualitative argument needs detailed examination, but if it is valid, we conclude that the net effect of waves generated equally in both directions will be to bring the mean flow toward solid body rotation, since whenever there is a westward jet at high latitudes it will be braked by the eastward waves which preferentially penetrate to high latitudes. An equal and opposite acceleration of course occurs at the equator.

Consider next the question of propagation distance. A wave of velocity 5 m s^{-1} requires 12 days to travel the radius of Venus. This is on the order of the radiative time constant near the one bar pressure level for disturbances of a few kilometers in size, so radiative damping is acceptably weak. Turbulent damping is a more difficult question. A marginally important eddy diffusion can be estimated from $K = k^{-2}t^{-1}$, with t

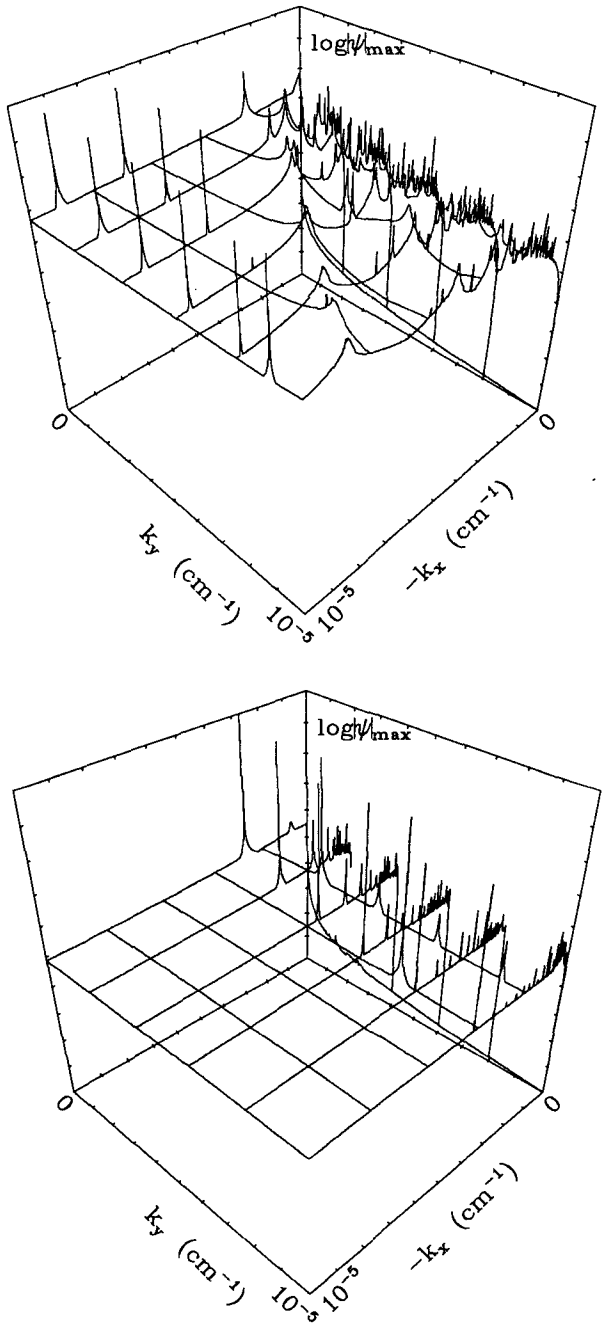

FIG. 10. Plots of $\log|\psi|_{max}$ for (a) $C = -67$ m s^{-1}, and (b) $C = 5$ m s^{-1}.

$= 12$ days and $k = 0.5 \times 10^{-5}$ cm^{-1}. This gives $K \sim 3 \times 10^4$ cm^2 s^{-1}. It seems possible that eddy diffusion within the ducts is this small. Clearly this is a very complicated question, however, since it involves the interaction of waves with the convection. It is even possible that there is positive feedback from the unstable layer.

We turn next to the amplitude question. Assuming that waves travel all the way from low latitudes to mid-latitudes, the magnitude of the acceleration they produce is uv/a, where a is the planetary radius. As a numerical example, if v and u are of order 3 m s^{-1}, we obtain $uv/a \sim 45$ m s^{-1} yr^{-1}. Hou and Goody (1989) have calculated the eddy or wave accelerations that must exist for consistency with the known mean zonal flow and radiative heating. They obtain about 40 m s^{-1} yr^{-1} at 60 km elevation, and about 10 m s^{-1} yr^{-1} at 50 km elevation. The principal momentum loss at the equator which must be balanced is the poleward transport due to the meridional cell at cloud level. According to their calculation, this involves a meridional flow velocity of $\bar{v} \sim 0.5$ m s^{-1} near 60 km elevation. With a zonal velocity difference of $\Delta\bar{u} \sim 10$ m s^{-1}, this cell produces a low latitude deceleration of $\bar{v}\Delta\bar{u}/a \sim 25$ m s^{-1} yr^{-1}. Note that the meridional velocities of the UV features, which are several m s^{-1}, represent motions at higher levels ($\sim$30 millibars pressure, at a height of $\sim$70 km).

A great deal more information is needed before firm conclusions can be reached, but it appears at least possible that large scale horizontal momentum exchange by small scale waves is important to the general circulation.

3. Advection hypothesis

In the advection hypothesis we explain the large-scale swirl pattern observed on Venus by the advection of small features formed at low latitudes. By integrating the average zonal and meridional wind profiles at a given time, the path of a small cloud feature can be calculated and compared to the cloud patterns observed on Venus. We assume that small features are advected with the local flow. Large scale albedo variations have been shown to propagate with a different velocity (Del Genio and Rossow 1990), but we do not address these features, only the small spots and striations which make up the swirl pattern.

a. Data set

The cloud patterns during five different years were studied using images from *Mariner 10* (1974) and *Pioneer Venus* (1979, 1980, 1982, 1983). The *Mariner 10* images are unmapped and can only be approximately compared to our calculated cloud patterns. The *Pioneer Venus* images are mapped onto a latitude and longitude grid where each pixel represents one-quarter degree of latitude and longitude. This projection allows direct comparison with calculated cloud patterns. The average zonal and meridional wind profiles used for the 1974, 1979, and 1982 imaging periods were those generated by Limaye et al. (1981, 1982, 1988) using tiepoints from image pairs. For the 1980 and 1983 im-

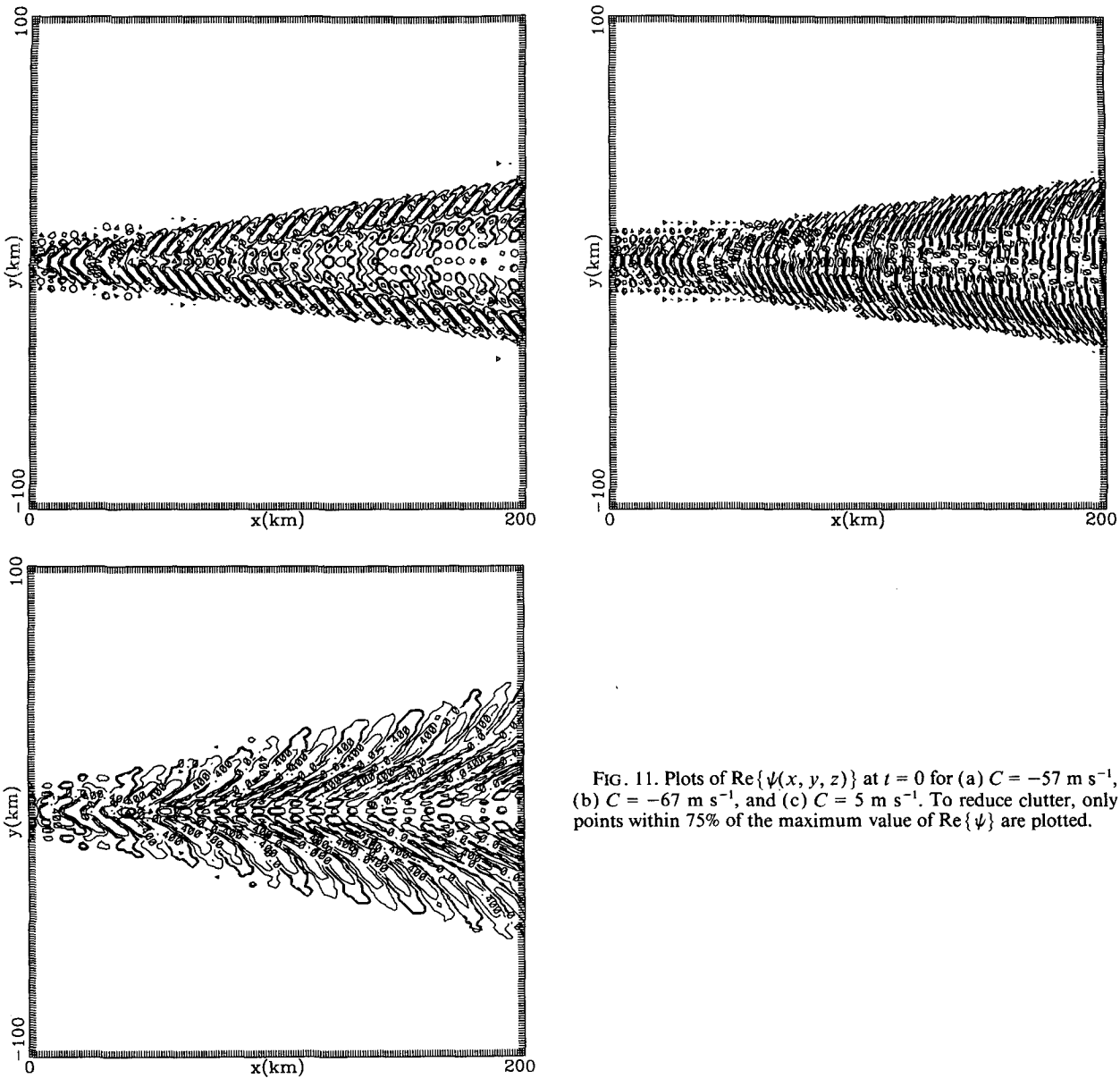

FIG. 11. Plots of $\mathrm{Re}\{\psi(x, y, z)\}$ at $t = 0$ for (a) $C = -57$ m s^{-1}, (b) $C = -67$ m s^{-1}, and (c) $C = 5$ m s^{-1}. To reduce clutter, only points within 75% of the maximum value of $\mathrm{Re}\{\psi\}$ are plotted.

aging periods, we generated our own wind profiles by collecting tiepoints from *Pioneer Venus* image pairs. The $u(\lambda)$ and $v(\lambda)$ for 1980 and 1983 are shown in Fig. 12. The data has been smoothed somewhat due to the relatively small number of tiepoints used to obtain these wind profiles. The wind profiles are not meant to be definitive measurements of the average winds during 1980 and 1983, but rather to show the constancy of the large-scale swirl pattern.

b. *Advection of features*

If the zonal and meridional winds [$u(\lambda)$ and $v(\lambda)$] are known for a range of latitudes λ, it is easy to integrate forward to find the path a test particle would follow in the wind:

$$\Delta\lambda = \frac{v(\lambda)\Delta t}{R}, \tag{15}$$

$$\Delta\phi = \frac{u(\lambda)\Delta t}{R\cos\lambda}, \tag{16}$$

where R is the radius of Venus.

To make our calculated paths more easily comparable to spacecraft images of Venus, we observe the motion of the test particle in a frame which corotates with the equatorial winds. This has the effect of subtracting out the solid-body component of the motion,

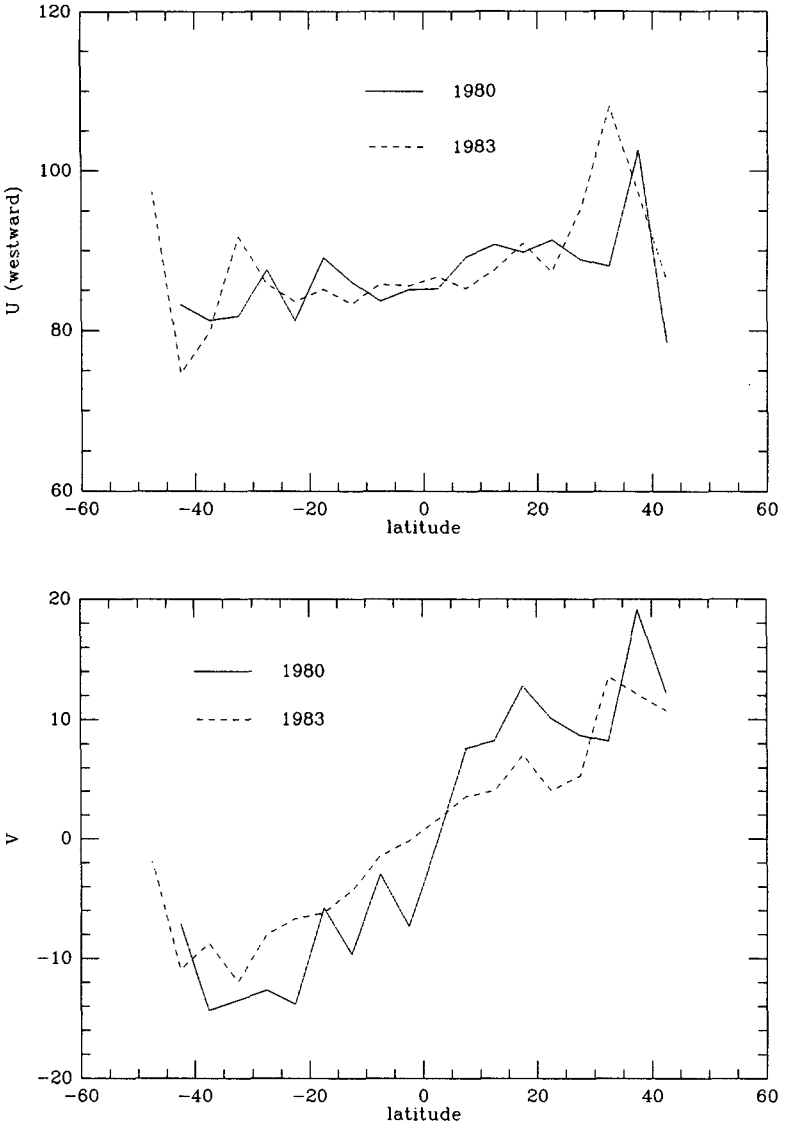

FIG. 12. Zonal (u) and meridional (v) wind velocities as a function of latitude used for the 1980 and 1983 imaging periods. The profiles have been smoothed somewhat due to the relatively small number of tiepoints used.

thereby showing the relative motions of test particles. The equation for $\Delta\phi$ is then replaced by

$$\Delta\phi = \frac{\Delta t}{R}\left[\frac{u(\lambda)}{\cos\lambda} - u(\lambda = 0)\right]. \qquad (17)$$

By starting particles at low latitudes and taking time steps of $\Delta t = 100$ minutes, we obtain the paths shown in Fig. 13. The test particle paths, or streamlines, are shown for each year where wind velocity data is available.

To study the advection of finite sized cloud features, we watch the motion of a number of test particles which lie on the perimeter of the cloud feature. Fig. 14 shows the results of this analysis. The cloud moves along the same path as the test particle and quickly shears out along the direction of its motion. Thus, small cloud features will soon become sheared out into streaks which lie along the streamlines of the mean flow. Larger clouds will also deform quickly to lie along streamlines, as will oblong clouds which begin perpendicular to the streamline. Images of Venus show a lack of circular features at mid latitudes and relatively few streaks at low latitudes. It is possible that all cloud features originate as small blobs at low latitudes and evolve into midlatitude streaks.

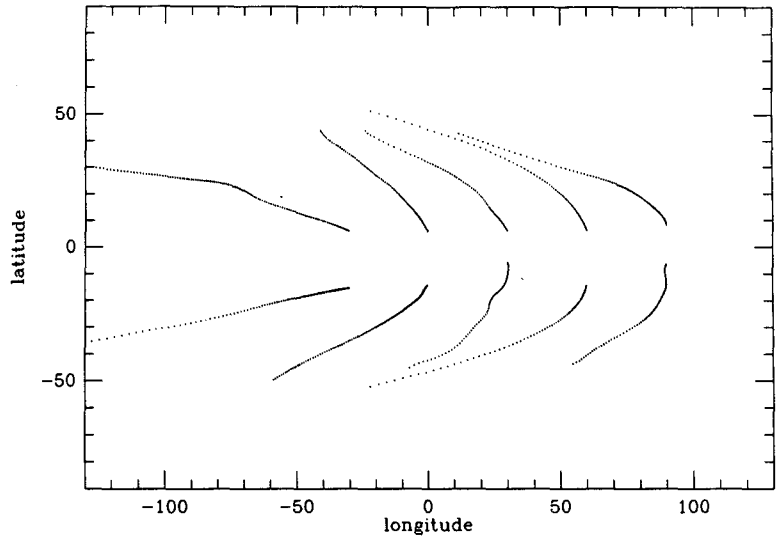

FIG. 13. Streamlines of test particles started out at low latitudes. From left to right, streamlines are for the 1974, 1979, 1980, 1982, and 1983 imaging periods. Time spacing between points on streamline is 100 minutes.

c. Results

In Fig. 15, streamlines are shown superimposed on representative images from each year of *Pioneer Venus* images. The streamlines have the same general appearance as the large-scale swirl pattern and show good agreement with the slope of the swirl pattern in most places. At some locations in the pictures it appears that there are cloud streaks at two different angles. The cause of the UV markings is not well understood, and this apparent crossing of cloud streaks could well represent two different levels in the atmosphere with different $u(\lambda)$ and $v(\lambda)$.

A direct comparison of streamlines with observed streaks of the kind done with *Pioneer Venus* images was not possible with the *Mariner 10* images since they have not been navigated or map projected. However, an approximate comparison was attempted by using a digitizing tablet to trace streaks on the 360 degree Venus mosaic given in Anderson et al. (1978, see their

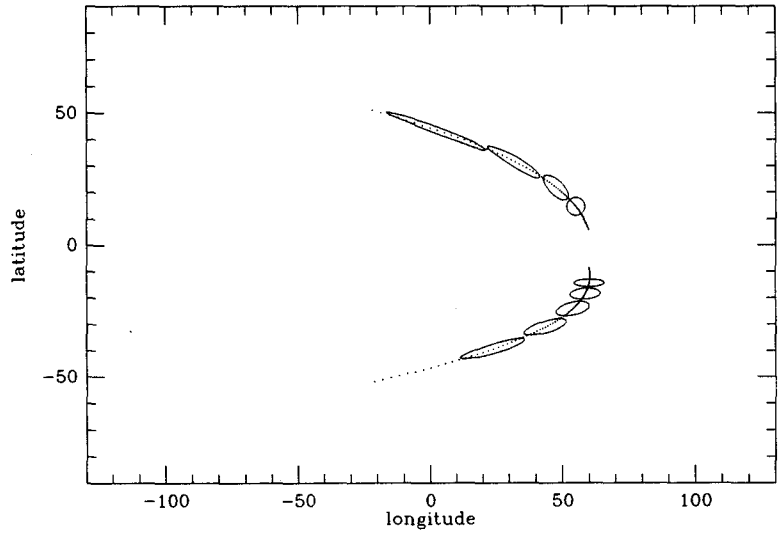

FIG. 14. The advection and shearing out of a finite sized cloud in each hemisphere is shown along with a streamline (dotted line) for the 1982 imaging period. Time spacing between drawings of cloud is approximately one day.

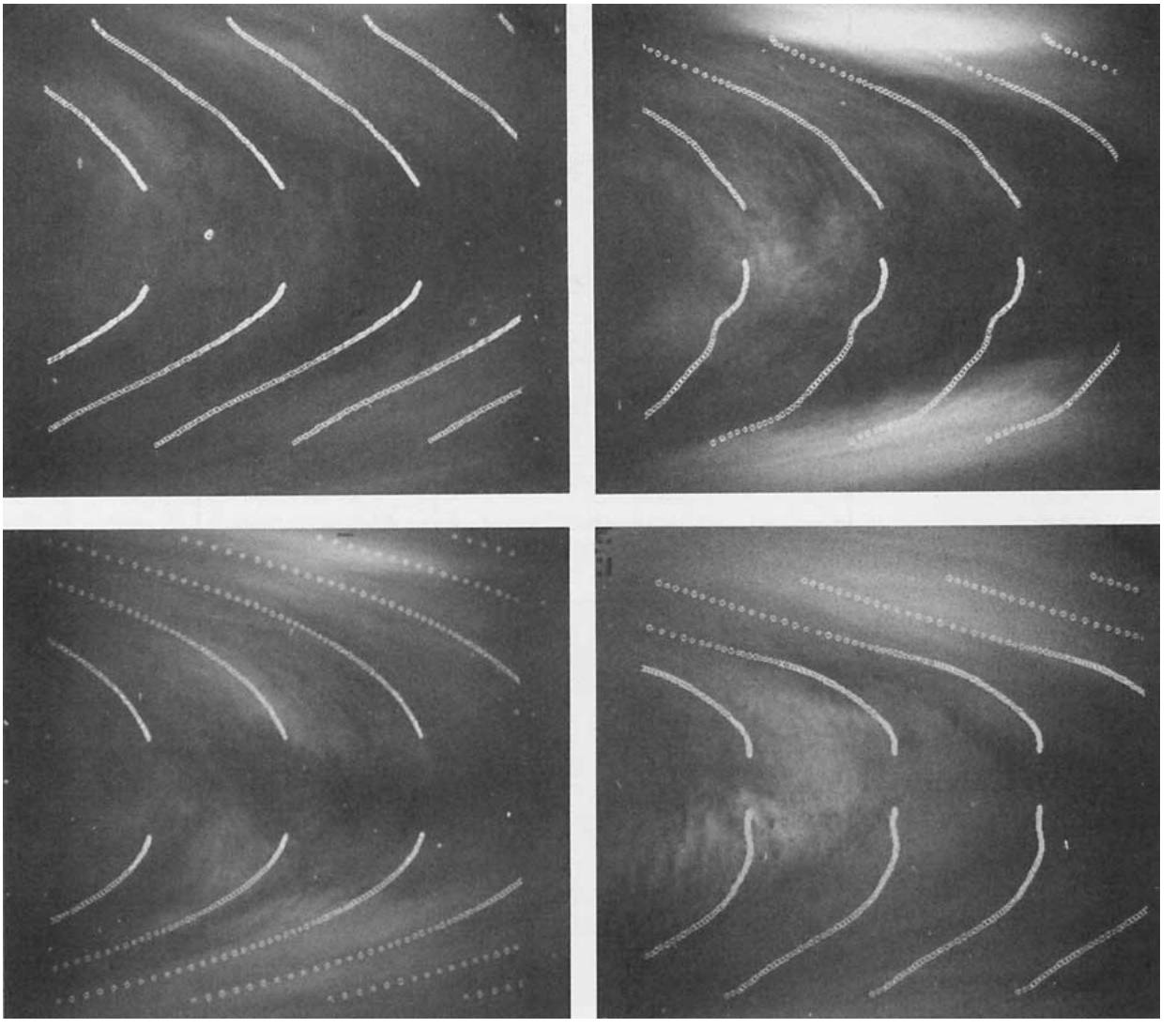

FIG. 15. Streamlines are shown superimposed on representative Pioneer Venus images from (a) 1979, (b) 1980, (c) 1982, and (d) 1983.

Compendium Plate 59). The results of this comparison are shown in Fig. 16 and again show general agreement between the slopes of the streaks in the swirl pattern and calculated streamlines.

The slope of a streamline is

$$\text{Slope} = \frac{\Delta\lambda}{\Delta\phi} = \frac{v(\lambda)\cos\lambda}{u(\lambda) - u(\lambda = 0)\cos\lambda}. \quad (18)$$

Thus, the shape of the swirl pattern is relatively insensitive to the details of $u(\lambda)$ and $v(\lambda)$. A swirl pattern similar to that seen on Venus will be caused by the advection of clouds as long as at midlatitudes $u(\lambda) > u(\lambda = 0)\cos\lambda$, and the meridional winds $v(\lambda)$, are poleward. These two conditions are always met on Venus during the period for which we have data.

The ultimate test of the advection hypothesis would be to track a small cloud feature from low latitudes for several days to see if it did in fact follow along the streaks in the swirl pattern. As indicated earlier, however, our analysis of the shearing of clouds shows that a cloud will deform rapidly and may become unrecognizable in as little as a day. This is consistent with the experience of ourselves and of others (Belton et al. 1976b) who have not been able to identify small features on successive four day rotations of the cloud deck. A cloud will typically move about five degrees in latitude in a day, so this type of analysis may be possible during the two days the cloud spends crossing the disk of Venus, especially with the higher temporal resolution images that Galileo should provide.

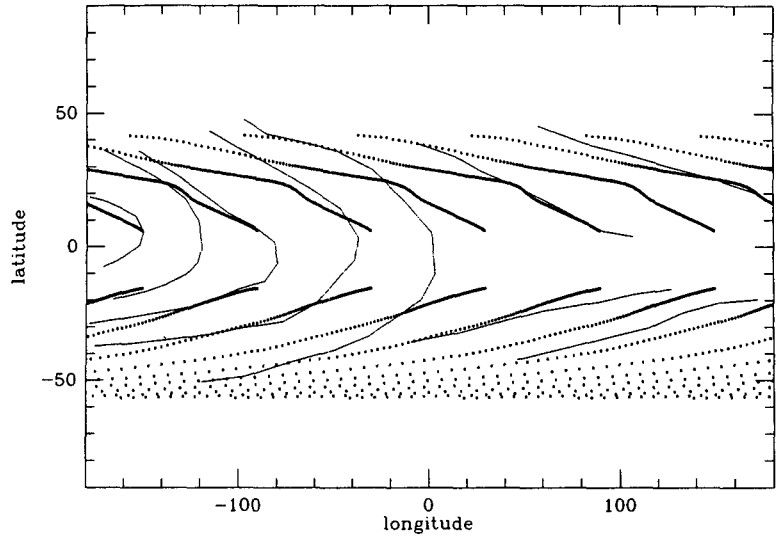

FIG. 16. Streamlines (regular pattern of thick lines and dots) are shown superimposed on streaks (thin lines) traced from a Mariner 10 composite image (Anderson et al. 1978, Compendium Plate 59).

4. Summary

In this paper we have investigated two different mechanisms for producing observed cloud top patterns in the atmosphere of Venus. We have demonstrated that ducted waves can exist in the atmosphere of Venus. These waves, existing at various levels in the atmosphere, may be the cause of some of the cloud features, and in addition, may have important dynamical effects on the atmosphere as a whole. We have also shown, however, that advection poleward of features created at low latitudes provides a simple explanation for the general appearance of the atmosphere with excellent agreement with observed cloud patterns. More definitive results await further theoretical work and observational tests.

Acknowledgments. We would like to thank A. Del Genio, A. Ingersoll, and J. Pollack for useful discussions. We thank A. Del Genio and W. Rossow for making available Pioneer images. This work was supported in part by NASA Grant NGL 33-010-186. PJS acknowledges the partial support of a Computational Research Associateship at the Cornell National Supercomputer Facility.

APPENDIX

Derivation of Equation (2)

In this Appendix, we provide the details of the derivation of (2). We take (1), write $\{\hat{\rho}, \hat{u}, \hat{v}, \hat{w}, \hat{T}\} = \{\bar{\rho}, \bar{u}, \bar{v}, \bar{w}, \bar{T}\} + \{\rho, u, v, w, T\}$ and expand to first order in the small quantities ρ, u, v, w, T. We obtain

$$u_{,t} + \bar{u}u_{,x} + w\bar{u}_{,z} + \frac{1}{\bar{\rho}}p_{,x} = f_x,$$

$$v_{,t} + \bar{u}v_{,x} + \frac{1}{\bar{\rho}}p_{,y} = f_y,$$

$$w_{,t} + \bar{u}w_{,x} + \frac{1}{\bar{\rho}}p_{,z} = -g\frac{\rho}{\bar{\rho}} + f_z,$$

$$\rho_{,t} + \bar{u}\rho_{,x} + w\bar{\rho}_{,z} + \bar{\rho}(u_{,x} + v_{,y} + w_{,z}) = 0,$$

$$\frac{1}{\bar{T}}(T_{,t} + \bar{u}T_{,x} + w\bar{T}_{,z})$$

$$-\frac{R}{c_p}\frac{1}{\bar{p}}(p_{,t} + \bar{u}p_{,x} + w\bar{p}_{,z}) = \frac{q}{\bar{T}},$$

$$\frac{p}{\bar{p}} = \frac{\rho}{\bar{\rho}} + \frac{T}{\bar{T}}. \tag{A1}$$

The last relation follows from the equation of state $\hat{p} = \hat{\rho}R\hat{T}$.

We now define $D \equiv \partial/\partial t + \bar{u}\partial/\partial x$ and $N^2 = (g/\bar{T}) \times (\partial\bar{T}/\partial z + g/c_p)$ (the Brunt-Väisälä frequency). Then, eliminating ρ using the equation of state, (A1) becomes

$$Du + w\bar{u}_{,z} + \frac{1}{\bar{\rho}}p_{,x} = f_x, \tag{A2}$$

$$Dv + \frac{1}{\bar{\rho}}p_{,y} = f_y, \tag{A3}$$

$$Dw + \frac{1}{\bar{\rho}}p_{,z} = -g\left(\frac{p}{\bar{p}} - \frac{T}{\bar{T}}\right) + f_z, \tag{A4}$$

$$D\left(\frac{p}{\bar{p}} - \frac{T}{\bar{T}}\right) + u_{,x} + v_{,y} + w_{,z} + \frac{\bar{\rho}_{,z}}{\bar{\rho}} w = 0, \quad \text{(A5)}$$

$$DT - \frac{\gamma - 1}{\gamma} \frac{\bar{T}}{\bar{p}} Dp + \frac{\bar{T}N^2}{g} w = q. \quad \text{(A6)}$$

Here we have used $R/c_p = (\gamma - 1)/\gamma$, where γ is the adiabatic index.

Now we use (A4) to eliminate T from (A5) and (A6), which become

$$(D^2 + N^2)w + \frac{g}{\gamma\bar{p}} Dp + \frac{1}{\bar{\rho}} Dp_{,z} = \frac{gq}{\bar{T}} + Df_z, \quad \text{(A7)}$$

$$D^2 w - g\frac{\bar{\rho}_{,z}}{\bar{\rho}} w - gw_{,z} - g(u_{,x} + v_{,y}) + \frac{1}{\bar{\rho}} Dp_{,z} = Df_z. \quad \text{(A8)}$$

Using (A2) and (A3), we may eliminate the term $u_{,x} + v_{,y}$ from (A8)

$$D^3 w - g\frac{\bar{\rho}_{,z}}{\bar{\rho}} Dw - gDw_{,z} + g\bar{u}_{,z}w_{,x} + \frac{g}{\bar{\rho}}(p_{,xx} + p_{,yy}) + \frac{1}{\bar{\rho}} D^2 p_{,z} = D^2 f_z + g(f_{x,x} + f_{y,y}) \quad \text{(A9)}$$

To proceed further, we now Fourier decompose the remaining independent variables w and p. We write $p(z, x, y, t) = \int p(z, k_x, k_y, \omega)e^{ik_x x + ik_y y - i\omega t} dk_x \times dk_y d\omega$, and similarly for w, $\mathbf{f}$, and q. In terms of the Fourier components $p(z, k_x, k_y, \omega)$, $w(z, k_x, k_y, \omega)$, (A7) and (A9) may be rewritten

$$(D^2 + N^2)w + \frac{g}{\gamma\bar{p}} Dp + \frac{1}{\bar{\rho}} Dp_{,z} = \frac{gq}{\bar{T}} + Df_z, \quad \text{(A10)}$$

$$D^3 w - g\frac{\bar{\rho}_{,z}}{\bar{\rho}} Dw - gDw_{,z} + ig\bar{u}_{,z}wk_x - \frac{g}{\bar{\rho}} p(k_x^2 + k_y^2) + \frac{1}{\bar{\rho}} D^2 p_{,z} = D^2 f_z + ig(k_x f_x + k_y f_y). \quad \text{(A11)}$$

In (A10) and (A11) $D = -i(\omega - \bar{u}k_x)$.

By combining (A10) and (A11), we can solve for p:

$$p = \frac{i\bar{\rho}(k_x f_x + k_y f_y) - \frac{\bar{\rho}D}{\bar{T}} q + N^2 \frac{Dw\bar{\rho}}{g} + D^2\left(\frac{\bar{\rho}w}{D}\right)_{,z}}{-k_x^2 - k_y^2 - \frac{D^2}{c^2}} \quad \text{(A12)}$$

where $c^2 = \gamma\bar{p}/\bar{\rho}$ is the sound speed squared.

Using (A12) in (A10), we get

$$(D^2 + N^2)\phi + \frac{g}{c^2}\left[\frac{N^2D^2}{g\mathcal{D}}\phi + \frac{D^2}{\mathcal{D}}\phi_{,z}\right] + \left[\frac{N^2D^2}{g\mathcal{D}}\phi + \frac{D^2}{\mathcal{D}}\phi_{,z}\right] = \frac{\bar{\rho}gq}{D\bar{T}} + \bar{\rho}f_z - \left(\frac{g}{c^2} + \frac{\partial}{\partial z}\right)\left[\frac{i\bar{\rho}}{\mathcal{D}}(k_x f_x + k_y f_y) - \frac{\bar{\rho}Dq}{\mathcal{D}\bar{T}}\right], \quad \text{(A13)}$$

where we have defined $\phi \equiv \bar{\rho}w/D$ and $\mathcal{D} \equiv -k_x^2 - k_y^2 - D^2/c^2$. Collecting terms, this becomes

$$\frac{D^2}{\mathcal{D}}\phi_{,zz} + \left[\left(\frac{D^2}{\mathcal{D}}\right)_{,z} + \left(\frac{N^2}{g} + \frac{g}{c^2}\right)\frac{D^2}{\mathcal{D}}\right]\phi_{,z} + \left[D^2 + N^2 + \frac{N^2D^2}{\mathcal{D}c^2} + \left(\frac{D^2N^2}{g\mathcal{D}}\right)_{,z}\right]\phi = \mathcal{R}, \quad \text{(A14)}$$

where $\mathcal{R}$ is the right hand side of (A13).

Note that $N^2/g + g/c^2 = -\bar{\rho}_{,z}/\bar{\rho}$, since $c_p = \gamma R/(\gamma - 1)$ and $\bar{p} = \bar{\rho}R\bar{T}$. Dividing (A14) by $D^2/\mathcal{D}$, and simplifying

$$\phi_{,zz} + \frac{\left(\frac{D^2}{\bar{\rho}\mathcal{D}}\right)_{,z}}{\left(\frac{D^2}{\bar{\rho}\mathcal{D}}\right)}\phi_{,z} + \left(\frac{\mathcal{D}}{D^2}\right)\left[D^2 + N^2 + \frac{N^2D^2}{\mathcal{D}c^2} + \left(\frac{D^2N^2}{g\mathcal{D}}\right)_{,z}\right]\phi = \frac{\mathcal{R}\mathcal{D}}{D^2}. \quad \text{(A15)}$$

Now we define $\psi \equiv (D^2/\mathcal{D}\bar{\rho})^{1/2}\phi$. Then

$$\psi_{,zz} + G\psi = F. \quad \text{(A16)}$$

Here

$$G = \frac{N^2 - \tilde{\omega}^2}{\tilde{\omega}^2}k^2 + \frac{\tilde{\omega}^2}{c^2} - \frac{N^2}{g}\frac{X_{,z}}{X} + \frac{N^2_{,z}}{g} - \frac{1}{4}\left[\frac{\bar{\rho}_{,z}}{\bar{\rho}} + \frac{X_{,z}}{X}\right]^2 + \frac{1}{2}\left[\frac{\bar{\rho}_{,z}}{\bar{\rho}} + \frac{X_{,z}}{X}\right]_{,z} \quad \text{(A17)}$$

where $\tilde{\omega} = \omega - k_x\bar{u}$, $X = (k^2/\tilde{\omega}^2 - 1/c^2)$, $k^2 \equiv k_x^2 + k_y^2$; and

$$F = \left(\frac{X}{\bar{\rho}}\right)^{1/2}\left\{\frac{\bar{\rho}gq}{D\bar{T}} + \bar{\rho}f_z - \left(\frac{g}{c^2} + \frac{\partial}{\partial z}\right) \times \left[\frac{i\bar{\rho}}{\mathcal{D}}(k_x f_x + k_y f_y) - \frac{\bar{\rho}Dq}{\mathcal{D}\bar{T}}\right]\right\}. \quad \text{(A18)}$$

REFERENCES

Anderson, J. L., M. J. S. Belton, G. E. Danielson, N. Evans and J. M. Soha, 1978: Venus in motion. *Astrophys. J. Supp. Ser.*, **36**, 275–284.

Belton, M. J. S., G. R. Smith, G. Schubert and A. D. Del Genio, 1976a: Cloud patterns, waves and convection in the Venus atmosphere. *J. Atmos. Sci.*, **33,** 1394–1417.

——, ——, —— and G. R. Smith, 1976b: Space-time relationships in the UV markings on Venus. *J. Atmos. Sci.*, **33,** 1383–1393.

Blamont, J. E., R. E. Young, A. Seiff, B. Ragent, R. Sagdeev, V. M. Linkin, V. V. Kerzhanovich, A. P. Ingersoll, D. Crisp, L. S. Elson, R. A. Preston, G. S. Golitsyn and V. N. Ivanov, 1986: Implications of the VEGA Balloon Results for Venus Atmospheric Dynamics. *Science,* **231,** 1422–1425.

Councelman, C. C., S. A. Gourevitch, R. W. King, G. B. Loriot and E. S. Ginsberg, 1980: Zonal and meridional circulation of the lower atmosphere of Venus determined by radio interferometry. *J. Geophys. Res.*, **85,** 8026–8030.

Del Genio, A. D., and W. B. Rossow, 1990: Planetary scale waves and the cyclic nature of cloud top dynamics on Venus. *J. Atmos. Sci.*, in press.

Gierasch, P. J., 1987: Waves in the atmosphere of Venus. *Nature,* **328,** 510–512.

Hou, A. Y., and R. M. Goody, 1989: Further studies of the circulation of the Venus atmosphere. *J. Atmos. Sci.*, **46,** 991–1001.

——, and B. F. Farrell, 1987: Superrotation induced by critical-level absorption of gravity waves on Venus: An assessment. *J. Atmos. Sci.*, **44,** 1049–1061.

Kawabata, K., D. L. Coffeen, J. E. Hansen, W. A. Lane, M. Sato and L. D. Travis, 1980: Cloud and haze properties from Pioneer Venus polarimetry. *J. Geophys. Res.*, **85,** 8129–8140.

Kerzhanovich, V. V., and M. Ya. Marov, 1983: The atmospheric dynamics of Venus according to Doppler measurements by the Venera entry probes. *Venus,* D. M. Hunten, L. Colin, T. M. Donahue, and V. I. Moroz, Eds., University of Arizona Press, 766–778.

Knollenberg, R. G., L. Travis, M. Tomasko, P. Smith, B. Ragent, L. Esposito, D. McCleese, J. Martonchik and R. Beer, 1980; The clouds of Venus: A synthesis report. *J. Geophys. Res.*, **885,** 8059–8081.

Leroy, S. S., and Ingersoll, A. P., 1989: Convective forcing of internal gravity waves and applications to the Venusian atmosphere. *Bull. Amer. Astron. Soc.*, **21,** 926.

Limaye, S. S., and V. E. Suomi, 1981: Cloud motions on Venus: Global structure and organization. *J. Atmos. Sci.*, **38,** 1220–1225.

——, C. J. Grund and S. P. Burre, 1982: Zonal mean circulation at the cloud level on Venus: Spring and fall 1979 OCPP observations. *Icarus,* **51,** 416–439.

——, C. Grassotti and M. J. Kuetemeyer, 1988: Venus: Cloud level circulation during 1982 as determined from Pioneer cloud photopolarimeter images. I. Time and zonally averaged circulation. *Icarus,* **73,** 193–211.

Press, W. H., B. P., Flannery, S. A., Teukolsky and W. T. Vetterling, 1986: *Numerical Recipes: The Art of Scientific Computing.* Cambridge University Press, 818 pp.

Rossow, W. B., A. D. Del Genio, S. S. Limaye, L. D. Travis and P. H. Stone, 1980: Cloud morphology and motions from *Pioneer Venus* images. *J. Geophys. Res.*, **85,** 8107–8128.

Schubert, G., 1983: General circulation and the dynamical state of the Venus atmosphere. *Venus,* D. M. Hunten, L. Colin, T. M. Donahue, and V. I. Moroz, Eds., University of Arizona Press, 681–765.

Seiff, A., D. B. Kirk, R. E. Young, R. C. Blanchard, J. T. Findlay, G. M. Kelly and S. C. Sommer, 1980: Measurements of thermal structure and thermal contrasts in the atmosphere of Venus and related dynamical observations: Results from the four Pioneer Venus probes. *J. Geophys. Res.*, **85,** 7903–7933.

Young, R. E., R. L. Waltersheid, G. Schubert, A. Seiff, V. M. Linkin and A. N. Lipatov, 1987: Characteristics of gravity waves generated by surface topography on Venus: Comparison with the VEGA balloon results. *J. Atmos. Sci.*, **44,** 2628–2639.